

Radio observations of the planetary nebula around the OH/IR Star OH 354.88-0.54 (V1018 Sco)

Martin Cohen¹, Jessica M. Chapman², Rachel M. Deacon^{3*}, Robert J. Sault²,
Quentin A. Parker^{4,5}, Anne J. Green⁶

¹*Radio Astronomy Laboratory, University of California, Berkeley, CA 94720, USA*

²*Australia Telescope National Facility, PO Box 76, Epping, NSW 2121, Australia*

³*School of Physics A28, University of Sydney, NSW 2006, Australia*

⁴*Anglo-Australian Observatory, PO Box 296, Epping, NSW 2121, Australia*

⁵*Department of Physics, Macquarie University, Sydney, NSW 2109 Australia*

⁶*Astrophysics Dept., School of Physics, Sydney University, Sydney, NSW 2006, Australia*

Accepted . Received ; in original form

ABSTRACT

We present radio observations of the unique, recently formed, planetary nebula (PN) associated with a very long-period OH/IR variable star V1018 Sco that is unequivocally still in its asymptotic giant branch phase. Two regions within the optical nebula are clearly detected in nonthermal radio continuum emission, with radio spectral indices comparable to those seen in colliding-wind Wolf-Rayet binaries. We suggest that these represent shocked interactions between the hot, fast stellar wind and the cold nebular shell that represents the PN's slow wind moving away from the central star. This same interface produces both synchrotron radio continuum and the optical PN emission. The fast wind is neither spherical in geometry nor aligned with any obvious optical or radio axis. We also report the detection of transient H₂O maser emission in this nebula.

Key words: masers - stars: AGB and post-AGB - planetary nebulae: general - radiation mechanisms: nonthermal

1 INTRODUCTION

Cohen, Parker & Chapman (2005: hereafter CPC) have reported the discovery of a very faint planetary nebula (PN) centred on the long-period pulsating OH/IR star OH 354.88-0.54, also known as

V1018 Sco. The PN was found during examination of survey field HA630 of the Southern H α Survey (SHS: Parker et al. 2005a) by QAP, as part of a systematic search for new Galactic Plane PNe (e.g. Parker et al. 2005b, 2006). Its OH characteristics mark this

star as an intermediate mass asymptotic giant branch (AGB) star, with initial mass $\geq 4M_{\odot}$. After rejecting the possibility that the PN arises from shock interaction with the surrounding external medium, or that the star is a “born-again” (e.g., Iben 1984) object that has undergone a very late thermal pulse (e.g., Blöcker & Schönberner 1997) as it began to evolve along its cooling track, CPC speculated that this object represents a phase of PN evolution that has been formerly unobserved. They concluded that this star’s fast wind has very recently turned on and it is the interaction between this wind and the previously shed outer layers of the star that produces the ionization that reveals the optical PN.

To explore this intriguing phenomenon further we have undertaken a series of radio continuum and water maser observations with the Australia Telescope Compact Array (ATCA), originally with the objective of mapping out the spatial distribution of ionized material within the PN. Pre-existing radio data are discussed in §2. §3 describes the new ATCA continuum and H₂O maser observations, while §4 shows an enhanced optical image of the PN. The discussion follows in §5, with our conclusions in §6.

2 PREVIOUS RADIO CONTINUUM OBSERVATIONS

The best estimate for the position of the star itself is: $17^h 35^m 02.73^s \pm 0.02^s$, $-33^{\circ} 33' 29.41'' \pm 0.24''$ (CPC). Neither the PMN or NVSS surveys includes any continuum source within several arcmin of OH 354.88-0.5, while the VLA survey of the inner plane at 5 GHz by Becker et al. (1994) is limited to $|b| \leq 0.4^{\circ}$. The 1.4-GHz continuum survey of small diameter sources by Zoonematkermani et al. (1990) does include a bright, compact radio object ($2.4''$ in size) within $7''$ of the maser position. However, this survey comprises two 3-MHz wide bands centred at 1441.5 and 1611.7 MHz, so the higher frequency band is contaminated by the strong 1612-MHz maser emission. This problem was recognized by White, Becker & Helfand (2005), who give an updated position at 20 cm of $17^h 35^m 02.590^s - 33^{\circ} 33' 31.18''$ (J2000) and warn of this contamination of their band-averaged flux densities. Zijlstra et al. (1989) quote an upper limit of 1.4 mJy at 2 cm from a VLA observation in September 1986.

Consequently, the only radio survey to have correctly de-

tected and assessed the continuum from OH 354.88-0.5 is the first Molonglo Galactic Plane Survey (MGPS1: Green *et al.* 1999), at 843 MHz. Extracting the individual MGPS1 images, from which the final survey images were constructed, shows a source at the maser position. Fitting a 2D-Gaussian to the object indicates an unresolved source with an 843-MHz flux density of 10.8 ± 0.6 mJy, located at $17^h 35^m 01.52^s - 33^{\circ} 33' 36.90''$ (J2000). The beam size of the Molonglo Observatory Synthesis Telescope at this location is $75''$ (N-S) by $43''$ (E-W) so the radio emission could occupy the full extent of the H α ring (roughly a $39''$ circle as shown by the images in §4) yet still be unresolved in MGPS1 images. Therefore, observations with the ATCA were planned.

3 NEW RADIO OBSERVATIONS

Short test observations were carried out with the ATCA in the continuum at 3 and 6 cm in December 2003 to determine whether emission could be detected. The ATCA has six 22-m diameter antennas with five of the antennas located on an east-west track of length 3 km. The sixth antenna lies 3 km further west giving a maximum baseline of 6 km. Further continuum observations were made at 3, 6, 13 and 20 cm in 2004–2005. Only OH and SiO masers were known for OH 354.88-0.54. Therefore, we investigated the H₂O maser line at 22235 MHz in November 2004 with a short observation that yielded a solid detection. We later followed up with a 12-h observation in June 2005 with the intention of imaging the water maser emission and to search for continuum emission at 22235 MHz.

Table 1 summarizes our new continuum observations. We refer to the observing bands as 1.35, 3, 6, 13 and 20 cm. The actual frequencies used were: 22235, 8640, 4800, 2368, and 1384 MHz. We used a phase centre of $17^h 35^m 02.73^s - 33^{\circ} 33' 19.71''$ (J2000) for the continuum observations, and $17^h 35^m 02.73^s - 33^{\circ} 33' 29.41''$ for the maser observations, corresponding to the stellar position. To correct for atmospheric amplitude and phase variations, the observations of the source were interleaved with short observations of a secondary calibrator source (1729-37 for 3, 6, 13 and 20 cm, and 1710-269 for 1.35 cm). The flux density scale and bandpass calibrations were applied from observations of the source

Table 1. Log of ATCA observations.

Date	Project	Config	Time	Bands cm	Cont/line	Bandwidth MHz	No.channels
08 Jan 2004	CX053	6A	6h	3,6	Continuum	128	32
14 Nov 2004	C1339	750C	~45min	1.35	H ₂ O maser	32	512
21 Dec 2004	C1339	1.5D	12h	3,6	Continuum	128	32
24 March 2005	C1339	6A	12h	13,20	Continuum	128	32
21 June 2005	C1339	6B	~12h	1.35	H ₂ O maser	16	512

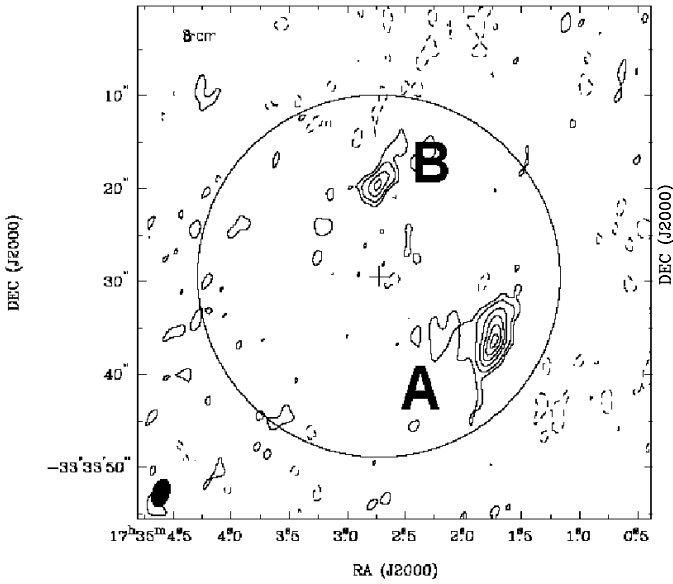


Figure 1. 3-cm ATCA continuum image of OH 354.88-0.54. The large circle indicates the approximate optical extent of the PN. The ring is 39'' in diameter, centred on the stellar position which is marked by the small cross. Radio contours plotted correspond to -4, -2, 2, 4, 8, 12, 16, 20 σ . 1σ is 0.04 mJy beam⁻¹. The beam size is shown in the bottom left corner.

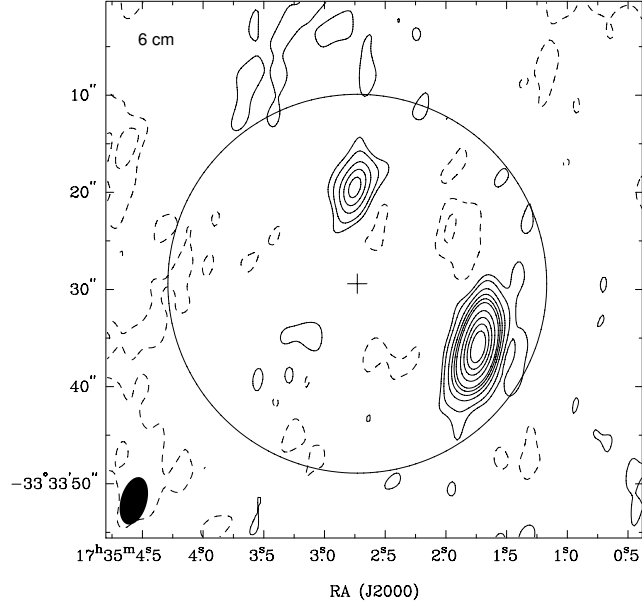


Figure 2. 6-cm ATCA continuum image of OH 354.88-0.54 as for Fig. 1. Radio contours plotted correspond to -4, -2, 2, 4, 8, 12, 16, 20, 30, 40, 50, 60 σ . 1σ is 0.03 mJy beam⁻¹.

1934-638 which is the primary flux calibrator for the ATCA. The resolutions achieved are given in column(4) of Table 2.

The 3, 6, 13 and 20-cm continuum images were made using natural weighting. All 3-cm data were used because there were no indications of broad scale Galactic emission. We cut out 6-cm data with uv-distances $< 2 \text{ k}\lambda$ to eliminate a low-level extended wash of Galactic emission and this radically improved the imagery. For the 13 and 20-cm data we excluded data with uv-distances $< 3 \text{ k}\lambda$. Figures 1, 2, 3 and 4 show the images with the position of the star and the approximate location of the outer optical edge of the PN also plotted.

Two obvious sources are detected within the PN at 3, 6 and 13 cm. The south western source (source A) is the stronger and is partially resolved with the resolution of the ATCA. The source to

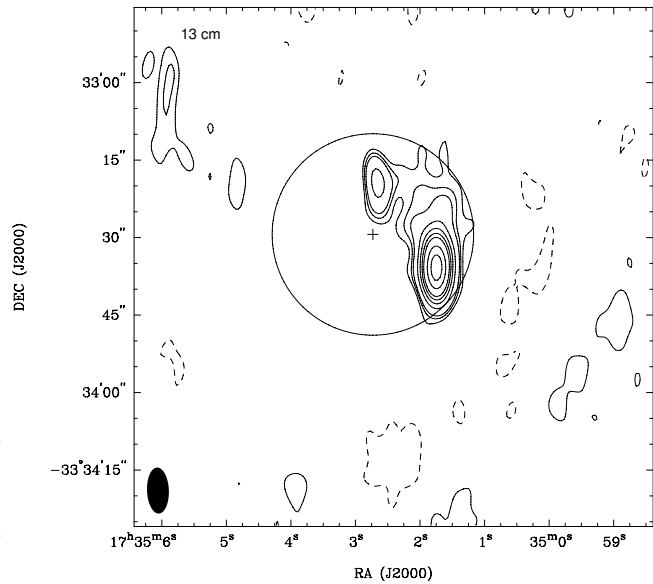


Figure 3. 13-cm ATCA continuum image of OH 354.88-0.54 as for Fig. 1. Radio contours have been chosen to emphasize a possible weak structure linking the two continuum components and correspond to -1.5, 1.5, 2, 3, 6, 8, 12, 14, 21, 30, 35 and 40 mJy beam⁻¹. 1σ is 0.14 mJy beam⁻¹.

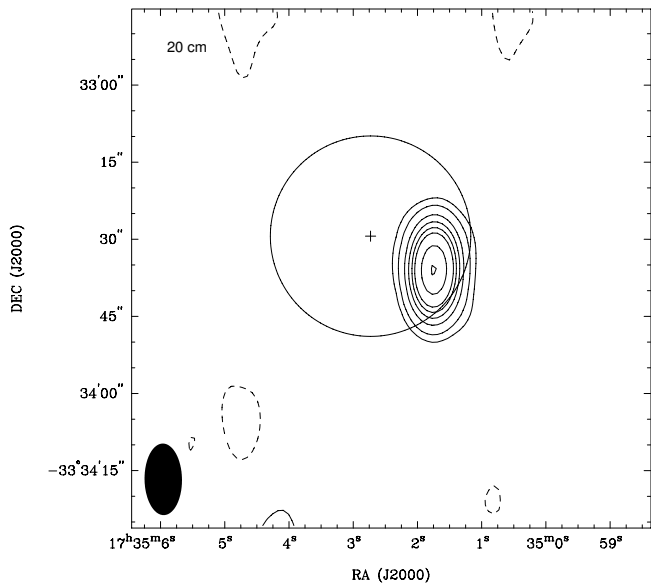


Figure 4. 20-cm ATCA continuum image of OH 354.88-0.54 as for Fig. 1. Radio contours plotted correspond to $-2, 2, 4, 8, 12, 16, 20\sigma$. 1σ is $0.18 \text{ mJy beam}^{-1}$.

the north of the stellar position (source B) is unresolved and significantly weaker, with no detection at 20 cm.

Table 2 presents the flux densities, positions, sizes and offsets from the star, for source A and source B at each wavelength. For source A, the size was estimated for each waveband by fitting a Gaussian and then deconvolving to remove the ATCA restoring beam. For source B, the Gaussian fitting was consistent in all cases with a point source.

A description of Table 2 follows: col.(1) gives the wavelength in cm; col.(2) the source; col.(3) the integrated flux density and its uncertainty; col.(4) the semiaxes and p.a. of the major axis for the beams used to deconvolve the images; col.(5) the same parameters as in col.(4) for the deconvolved sources; col.(6) the best-fit positions to the Gaussians; and col.(7) the modulus of the vector distance between each source and the central star. Our upper limits are 5σ values.

Source A has a definite nonthermal spectrum with the detected flux density falling with increasing frequency. The 20-cm detection of 7.7 mJy is comparable to the $10.8 \pm 0.6 \text{ mJy}$ detection of the MGPS1 object (Fig. 5). Therefore, we associate A with the 843-MHz (35-cm) source. In Figure 5, inverse-variance weighted least squares fits to power laws are plotted for sources A and B. Both sources have strongly nonthermal spectra ($F_\nu \propto \nu^{\text{index}}$) with in-

dices of -0.81 ± 0.01 and -0.95 ± 0.11 respectively, probably due to synchrotron emission. Fitting just the four ATCA data points for source A still yields a slope of -0.81 ± 0.01 , indistinguishable from the power law fit including the MGPS1 datum, vindicating our identification of source A as the 843-MHz source. The power law fitted to A is also consistent with the VLA 2-cm upper limit obtained by Zijlstra et al. (1989) and our own limit on continuum at 1.35 cm (see below).

Source B is much weaker than A, but the slope of the radio continuum emission is defined by robust detections at 6 and 13 cm. Source B appears to suffer substantial absorption at 20 cm (Fig. 5) which we interpret as free-free absorption. This absorption is likely to occur within the volume of the PN suggesting that source A is seen on the front of the nebula while source B is seen at the back.

The 3-cm flux density of 0.60 mJy detected for source B is somewhat higher than that expected for synchrotron emission alone (0.31 mJy). (We did not include this point in the derivation of the spectral index for B because of the high significance of the deviation from the slope.) We interpret this detection as indicating the likely presence of some additional weak thermal radio emission (§5).

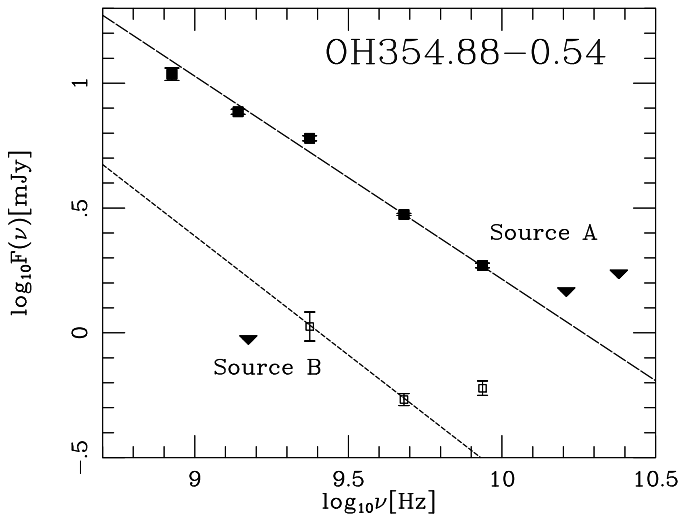
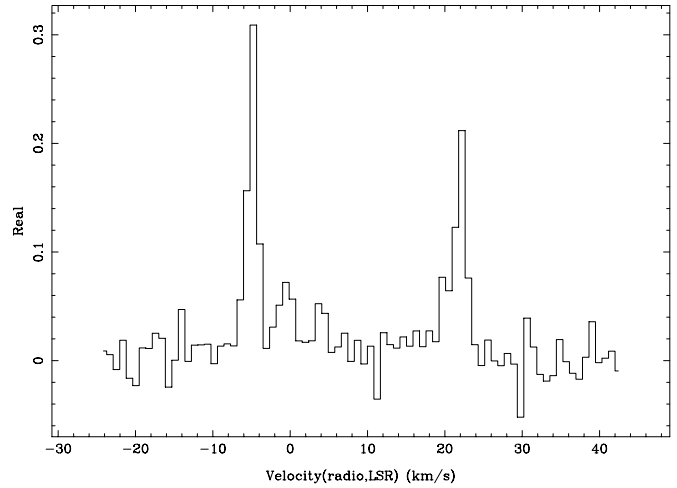
In Figure 3, a weak structure appears to provide a link between sources A and B at 13 cm (Fig. 1). However, this is only a 2σ detection and is not confirmed. There is no evidence for diffuse radio continuum emission filling the entire PN.

The projected mean distances from the stellar position to the peaks of sources A and B are the same, within the uncertainties: $10.4 \pm 0.7''$ (A) and $9.9 \pm 0.8''$ (B).

Figure 6 represents the discovery of H_2O maser emission from OH 354.88-0.54, from a 40-minute observation taken in November 2004. Two peaks are seen at velocities (LSR) of -4.8 and $+22.2 \text{ km s}^{-1}$, significantly displaced by $1-2 \text{ km s}^{-1}$ from the corresponding OH maser peaks (-5.5 and $+24.3 \text{ km s}^{-1}$, respectively: CPC). The blue peak is the stronger with a flux density of 0.31 Jy ; the red peak has a flux density of 0.21 Jy . From these limited data we were unable to measure the maser positions. We can infer only that we observed two blobs of water maser emission, but we cannot interpret the peak velocity differences in terms of relative locations of the masing species. It is also noteworthy that the water maser

Table 2. Summary of best-fit continuum results to single Gaussians for sources A and B.

Band cm	Source	Total flux \pm rms mJy	Restoring beam semi-axes (arcsec)(deg)	Deconvolved size (arcsec)(deg)	Best-fit Position	Offset from star arcsec
1.35	...	<1.65	1.1 \times 0.6		No continuum detected	
3	A	1.86 \pm 0.04	3.0 \times 1.83(-20.9)	4.48 \times 1.39(-12.8)	17:35:01.74 -33:33:36.0	10.5 \pm 1.4
6	A	2.98 \pm 0.03	5.1 \times 2.7(-15.7)	4.4 \times 0.84(-12.5)	17:35:01.74 -33:33:35.9	10.5 \pm 1.4
13	A	6.02 \pm 0.14	9.3 \times 4.5(2.3)	6.0 \times 1.9(-1.6)	17:35:01.75 -33:33:35.6	10.2 \pm 1.4
20	A	7.68 \pm 0.18	13.9 \times 7.3(0.9)	2.8 \times 0.65(-41)	17:35:01.74 -33:33:36.0	10.5 \pm 1.4
3	B	0.60 \pm 0.04	3.0 \times 1.83(-20.9)	Point source	17:35:02.73 -33:33:19.3	10.1 \pm 1.4
6	B	0.54 \pm 0.03	5.1 \times 2.7(-15.7)	Point source	17:35:02.75 -33:33:19.5	10.0 \pm 1.4
13	B	1.06 \pm 0.14	9.3 \times 4.5(2.3)	Point source	17:35:02.64 -33:33:19.7	9.7 \pm 1.4
20	B	<0.90	13.9 \times 7.3(0.9)	Point source	No continuum detected	


Figure 5. Spectral energy distributions of sources A and B fitted by power laws. Filled triangles indicate upper limits at 2 cm from the VLA and 1.3 cm from our data for A, and at 20 cm, from our data, for source B.

Figure 6. Spectrum of H₂O maser emission detected from the PN.

profile is significantly above zero in the centre, similar to the OH profile (CPC).

Despite the 12-h track obtained during the June 2005 ATCA observation, we had a non-detection of any water maser emission with a 5σ limit of ~ 40 mJy. Extrapolating from Figure 3 of CPC we estimate that we detected water masers at an OH maser phase of 0.57 but failed at a phase of 0.72. This interval is such a small fraction of a period that the source must be highly variable and the water masers clearly do not follow the very regular OH maser variations. The range of variation in H₂O maser intensity from the 2004 to the 2005 observation was about a factor of 8. We looked for radio continuum emission at 1.35 cm using the spectral line data but achieved no detection, with a 5σ upper limit of 1.65 mJy.

4 OPTICAL IMAGERY

Figure 7 represents a quotient map obtained directly from SuperCOSMOS data for the PN by dividing the H α pixel data by the corresponding data from the short-red (SR) exposure. However, it also involves use of the Bond et al. (2002) technique of variable point-spread-function (PSF) matching between the two images prior to division. This enhances the faint nebula by effectively removing most of the emission from point sources in the field. The figure shows that the outer boundary of the PN is quite sharply defined around most of its circumference. Emission can clearly be seen above the sky over most of its projected area although the brightening of the south-eastern region is particularly striking. There is also the suggestion of a northward extension although this is very faint and merges imperceptibly with the interstellar medium (ISM). The north-south extent could be as much as 20% greater than the east-west diameter in this newly processed image. Fig. 8 shows the

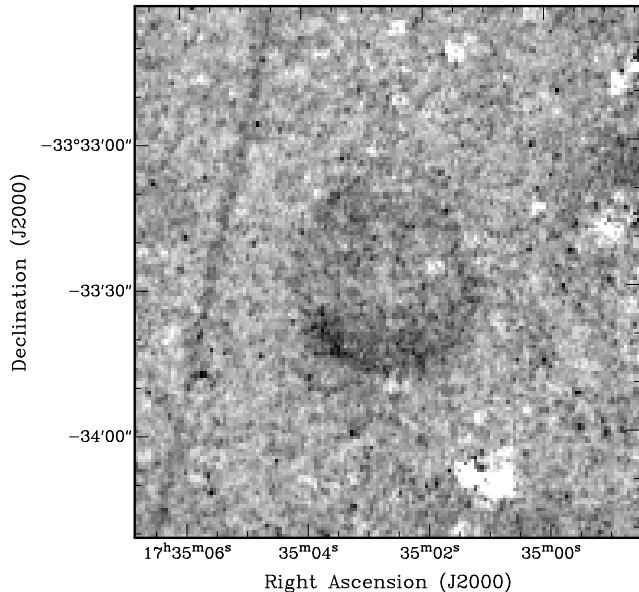


Figure 7. $H\alpha$ /SR quotient image of the PN with variable PSF-matching before dividing the $H\alpha$ and SR data. The linear feature east of the PN is the track of a satellite.

relationship between sources A and B and the PN in the plane of the sky.

An old UKST $H\alpha$ plate which includes the PN region exists in the archive. This exposure (HA2307) was taken in 1976 for John Meaburn on fast but coarse-grained O-9804 emulsion with a mosaic $H\alpha$ filter. The enhanced south-east section of the PN is clearly visible on this old exposure but the remaining boundary is hard to discern. This, coupled with the poorer resolution of this exposure, make it essentially impossible to measure whether there has been any expansion of the nebula ring over the intervening 20-plus years.

5 DISCUSSION

Nonthermal emission from early-type stars was found in Wolf-Rayet stars (WRs) by Abbott, Biegging, & Churchwell 1984; Abbott et al. 1986; Biegging et al. 1989). Its origin lies in the acceleration, by strong shocks, of a small population of relativistic electrons (White 1985). In WR binary systems these shocks arise from the collision of the separate winds of the two components. It is less certain whether the phenomenon occurs in single WR stars. The paradigm applied to OH 354.88-0.54 involves a single star but two stellar winds from different phases of evolution. Absorption of

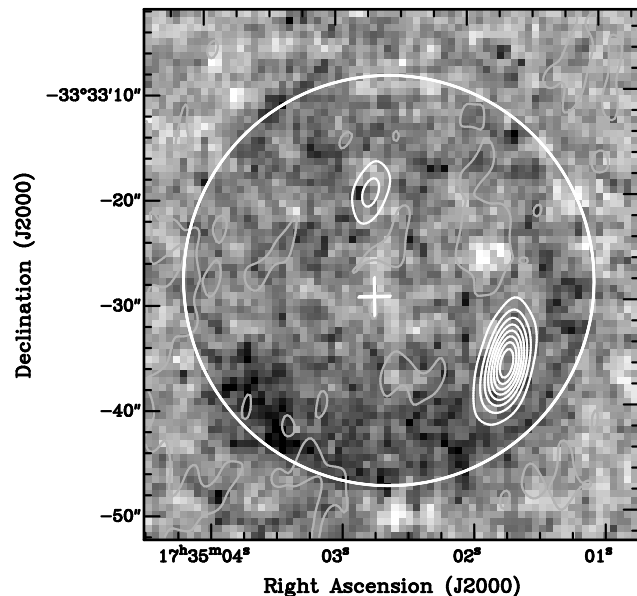


Figure 8. An enlarged version of Fig. 7 overlaid by white contours of 6-cm radio continuum emission corresponding to 0.3, 0.5, 0.8, 1.1, 1.4, 1.6, 1.9, 2.2 mJy beam^{-1} . White circle marks the approximate outer boundary of the PN; cross marks the position of the star and OH masers.

synchrotron emission has been observed in colliding winds from WRs by Chapman et al. (1999), who attributed this to thermal absorption by gas along the line-of-sight through the ionized wind. The observed continuum energy distribution for WR 48 (Chapman et al. 1999, Fig. 11) reveals nonthermal emission between 3 and 13 cm but only an upper limit at 20 cm, implying a pronounced turnover longward of ~ 13 cm. These authors separated the thermal and nonthermal contributions to the spectrum of WR 48 and found the nonthermal component to have a slope of -0.83 . This slope matches that for OH 354.88-0.54 sources A and B (within the errors), strongly suggesting that we may be viewing nonthermal emission in this PN that is also caused by the collision of two winds, the low density, high velocity PN fast wind and the high density, slowly moving original PN ejecta. Synchrotron self-absorption is unimportant in sources with brightness temperature below 10^{10} K (Condon 1992) but thermal absorption within the PN is still relevant and could cause the abrupt turn-down in the spectrum of source B. Locating source A near the front side of the PN, as we view it, would account for the lack of absorption in its radio spectrum.

5.1 Estimates of electron density

The PSF-subtracted image of the PN (Fig. 7) indicates that the $H\alpha$ brightness varies significantly across the PN suggesting that the electron density also varies. It is also possible that the southern rim of the PN is brightest because the PN's slow wind suffers a shock at the interface with the ISM. Source A lies within the western portion of the brightest (southern) region of $H\alpha$ emission, for which CPC determined $N_e \sim 4000 \text{ cm}^{-3}$, whereas B appears in an area of much lower $H\alpha$ brightness to the north (Fig. 7). We can use the turnover in source B's radio spectrum to estimate the mean electron density through the nebula in its direction. The thermal optical depth through the nebula may be calculated following Mezger & Henderson (1967, eqn (5)), and rearranged into an expression for the turnover frequency (in GHz), $\nu_T \approx 0.3(T_e^{-1.35} N_e^2 L)^{0.5}$ (Lang 1999, eqn.1.224), where L is the path length through the PN in pc (we adopt the diameter of the PN, $1.9 \times 10^{18} \text{ cm}$, 0.6 pc, for L: note that CPC's Table 1 gave the diameter as 0.3 pc; this was in fact the radius). The turnover wavelength must lie beyond 13 cm but be less than 20 cm, so ν_T must lie between 1.5 and 2.3 GHz. Taking $T_e \sim 10^4 \text{ K}$, we conclude that the mean nebular N_e along the line-of-sight toward B is between 3200 and 4900 cm^{-3} , in excellent agreement with the density derived from the [SII] lines (4000 cm^{-3} ; CPC).

5.2 Possible free-free emission in source B

We also consider whether the apparent excess of 3-cm emission in B, above the nonthermal slope, might be due to free-free emission, as seen in WR stars. Firstly we have separately analyzed the two 3-cm data sets to investigate the reality of this excess by fitting a point source to the calibrated u-v data. This should give a more reliable flux estimate than fitting in the image plane, if there were no confusion and the emission were unresolved. We find $0.61 \pm 0.03 \text{ mJy}$ (Jan 2004) and $0.59 \pm 0.03 \text{ mJy}$ (Dec 2004), where the errors are the rms residuals from the fitting process alone. Our measurement of the same value at two epochs separated by nearly a year gives strong support for the reality of the measured flux density. Extrapolating source B's nonthermal spectrum to 3 cm implies a level of

0.31 mJy. Therefore, we conclude that B shows a real excess at 3 cm of 0.29 mJy.

To estimate the expected radio free-free level we have applied an absolute calibration to the $H\alpha$ image of the nebula according the method described by Pierce (2006), in which a scaled continuum (SR) image is subtracted from the $H\alpha$ image, and a factor is applied to relate the SHS difference image to the spatially much lower-resolution, but absolutely calibrated, Southern $H\alpha$ Sky Survey Atlas (SHASSA: Gaustad et al. 2001). For this PN, the SR scale is 0.99 and the conversion factor in this field is 14.9 counts pixel^{-1} per Rayleigh. Integrating the entire PN spatially, subtracting background sky (assessed as the average of that measured in four different locations to provide a robust background) and three point sources interior to, or on the rim of, the nebula, and after correction for the 36% contribution of the red [NII] line to the emission in the bandpass of the SHS $H\alpha$ filter, we derive 3.6 Rayleighs in $H\alpha$ alone. This is equivalent to $2.4 \times 10^{-14} \text{ erg cm}^{-2} \text{ s}^{-1}$. We now require the total extinction to the PN. Based on Fitzgerald (1968), Lucke (1978) and especially on Neckel & Klare (1980), we find $A_V \approx 3.5$ in this direction, corresponding to $A_{H\alpha} \approx 2.8$. Thus the intrinsic $H\alpha$ flux is $3.3 \times 10^{-13} \text{ erg cm}^{-2} \text{ s}^{-1}$, and the corresponding $H\beta$ flux would be $1.1 \times 10^{-13} \text{ erg cm}^{-2} \text{ s}^{-1}$.

This is convertible into the radio free-free flux density using Condon (1992: eqns. (3) and (4a)). The estimated free-free emission at 3 cm, for the entire nebula, is 0.33 mJy and this is comparable to the excess emission detected at 3 cm. Source B was unresolved and thus only occupies a small part (less than about 2%) of the nebular area. For a uniform distribution the predicted free-free emission from source B would be less than 0.01 mJy. However, one would expect the radio thermal emission to follow the $H\alpha$ brightness distribution and, therefore, to be patchy. There is precedent for this in the Luminous Blue Variable HD 168625 (Leitherer et al. 1995), where the radio continuum shell closely mimics the morphology of the partially filled $H\alpha$ shell. If the free-free emission were highly clumped toward source B, then a larger fraction of the total thermal emission might be concentrated there. Alternatively, if our line-of-sight to source B through the PN suffered significant internal extinction then the estimated intrinsic $H\alpha$ emis-

sion would also increase. Consequently, local overdensities of ionized gas could be offset by internal nebular extinction due to dusty clumps. For example, if 20% of the total observed free-free emission were located within source B (an overdensity greater than a factor of 10), and there were an extra extinction (A_V) of 2.1 magnitudes ($A_{H\alpha}$ of 1.7 mag) within the nebula, then radio free-free emission of 0.3 mJy would still be observed. (In this case the total PN free-free emission would be 1.65 mJy, boosting the intrinsic Balmer line fluxes by $\times 5$, requiring a line-of-sight $A_{H\alpha}$ of 4.6, equivalent to an A_V of 5.6 mag, of which 3.5 mag arise from the ISM and 2.1 mag within the PN.)

The upper limit on B at 20 cm also excludes a cut-off in the electron energy spectrum because there is no intermediate regime with $S_\nu \propto \nu^{1/3}$ between the optically thin and thick spectral indices (Ginzburg & Syrovatskii 1965). The fact that A and B have almost the same nonthermal slope strengthens the case for either a common volume in which we observe this nonthermal emission, or two separated volumes in which very similar strong shocks generate relativistic electrons. The fast wind, therefore, must encounter essentially the same physical conditions at the two locations in which it impacts the nebular ejecta.

5.3 Background source contamination

Both sources A and B are located within the ring and no other strong background objects are apparent. One can ask whether sources A and B are truly associated with the PN or might represent a double radio source viewed by chance along the line-of-sight. Inspection of our observed images covering the ATCA primary beams at 20 cm (~ 1000 arcmin²) and 6 cm (~ 80 arcmin²) suggests that 7 and 3 sources, respectively, are recognizable above the noise, at all flux densities, and none appear double. Calculating the formal extragalactic confusion from Log N–Log S relationships at 20 and 6 cm (Ledden et al. 1980; Bridle 1989) one would expect to detect 15 radio sources within the ATCA primary beam at 20 cm with a flux density greater than the sum of A and B, but less than one similarly within the 6-cm primary beam. The probabilities of even a single background source as bright as A appearing within the PN $H\alpha$ image are approximately 1/500 (6 cm) and 1/200 (20 cm). There

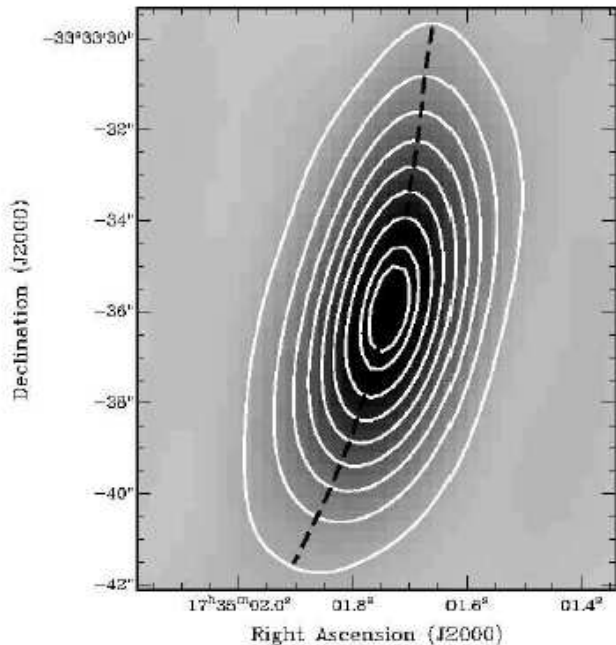


Figure 9. 6-cm continuum emission of source A shown both as a greyscale image and overlaid by its own contours in white, for levels of 0.2, 0.4, 0.7, 0.9, 1.2, 1.4, 1.6, 1.85, and 2.0 mJy beam⁻¹. The black dashes mark the locus of the ends of the major axes of the white contours. Note the distinct curvature of this locus.

are several other arguments that imply a physical linkage with the PN: they have statistically the same nonthermal radio spectral indices instead of the more common thermal sources found along the Galactic plane; there may be a faint connection between the emission of A and B; and A lies very close to the edge of the PN and is clearly curved, roughly concentrically, with the rim (Fig. 9), making a physical interaction between A and the ejecta that define the PN rim highly plausible.

5.4 Radio luminosity and kinetic energy: comparison with WR stars

We have compared our continuum observations at different epochs and see no indications of variability at any of the wavelengths observed over a period of 1.5 yr. Chapman et al. (1999: their Table 3) tabulated the monochromatic 6-cm luminosity of WRs that emit nonthermal radio emission. The average of the 9 WRs detected was $2.1 \pm 0.6 \times 10^{19}$ ergs s⁻¹ Hz⁻¹. The same calculation yields 3.7 and 0.7×10^{19} ergs s⁻¹ Hz⁻¹ for A and B, respectively. Summing the two nonthermal sources in OH 354.88-0.54, the PN is more luminous than the average nonthermal WR emitter. Adding A and B we find that the approximate nonthermal radio luminosity

(for an adopted bandwidth of 10 GHz; cf. Chapman et al. 1999) is 4.4×10^{29} ergs s^{-1} Hz $^{-1}$. High energy emission is detected from some WRs in which colliding winds occur. OH 354.88-0.54 has not been detected based on a search of X-ray and γ -ray catalogues. In particular, Chandra has not observed in its direction.

We now compare OH 354.88-0.54 with WR stars, for which a typical radio luminosity is a few $\times 10^{29}$ ergs s^{-1} . The total kinetic energy (KE) flux calculated from the known mass loss rates (\dot{M}) of WRs (a few $\times 10^{-5}$ M_{\odot} yr $^{-1}$) and wind velocities ($V_{wind} \sim 2000$ km s^{-1}), $\frac{1}{2} \dot{M} V_{wind}^2$, is typically 6×10^{37} ergs s^{-1} . For a WR–O-star collision about 0.3% of the flux passes through the interaction region, so the KE flux at the interaction is about 2×10^{35} ergs s^{-1} (see Chapman et al. (1999) for details).

For the detected continuum sources A and B, the 5-GHz radio luminosity is 4.4×10^{19} ergs s^{-1} Hz $^{-1}$ and the total integrated radio luminosity (L_{radio}) is thus about 4.4×10^{29} ergs s^{-1} . We assume that the ratio of KE flux/radio luminosity is the same as for WR stars (about $10^6:1$). Thus approximately 4.4×10^{35} ergs s^{-1} should be available at the shock regions. By comparison with WR binaries, the total KE flux of the fast wind of OH 354.88-0.54 is not well determined as we do not know what fraction of the fast wind encounters the shocked regions. Source A occupies about 1/100 of the total shell area (estimated at 6 cm) while source B is smaller. For a smooth distribution this suggests that the KE could be about $100\times$ higher than at the shock. However, if the fast wind is clumpy or asymmetric then this is likely to be considerably overestimated.

As an example, we consider a scenario where 10% of the total KE flux reaches the detected shocked regions giving a total KE flux of 4.4×10^{36} ergs s^{-1} . For V_{fast} , the velocity of the fast wind, we adopt 1000 km s^{-1} . From these values we can crudely estimate the mass-loss rate of the fast wind to be $\dot{M}_{fast} \approx 1.2 \times 10^{-5} M_{\odot}$ yr $^{-1}$.

We now estimate the velocity of the compressed shell (V_{shell}) for this mass-loss rate. From eqn.(9) of Zijlstra et al. (2001) and using $\dot{M}_{agb} = 7 \times 10^{-5}$, $V_{agb} = 15$ km s^{-1} , $\dot{M}_{fast} = 1.2 \times 10^{-5}$, and $V_{fast} = 1000$ km s^{-1} , we have $\mu = 0.17$ and $\xi = 67$, where $\mu = \dot{M}_{fast}/\dot{M}_{agb}$ and $\xi = V_{fast}/V_{agb}$. For these values the velocity of the compressed shell is ~ 60 km s^{-1} and this can be compared to the observed line-of-sight optical velocity of 20 km s^{-1} . If less than 10% of the total energy flux reaches the shocked regions then

both \dot{M}_{fast} and V_{shell} would be higher while, if a larger fraction of the energy flux were intercepted, then \dot{M}_{fast} and V_{shell} would be lower.

5.5 Wind interactions

Despite the roughness of these estimates they do provide an idea of the relevant interactions. The fast wind ploughs into the slow AGB wind creating shocks, non-thermal emission and a compressed shell on the inner face. If the fast wind has a momentum ($\dot{M}_{fast} \times V_{fast}$) that is roughly comparable to (or greater than) that of the slow wind then, when they collide, the slow wind is compressed and accelerated and this increase in velocity is indicated by the velocity of the optical emission. The shock excitation must be stronger in the compressed intranebulular shell than at the ISM and the rather high density derived from the red [SII] doublet is more suggestive of a post-shocked region rather than a typical PN envelope. Therefore, it is more likely that the optical emission in the PN arises at the interface of the fast wind and AGB wind, rather than at the interface of the AGB wind and the ISM.

The geometry of the emerging fast wind is unknown because any spherically symmetric flow from the star would be immediately modified by its encounter with the dense circumstellar OH toroid. Naively, were this toroid to constrain the fast wind to the polar directions (north-south) in which OH maser emission is weakest (Welty, Fix & Mutel 1987), one might expect to see nonthermal ‘‘hot spots’’ in two opposing directions. There is evidence of a $10\text{-}\mu\text{m}$ source around the star that is significantly elongated north-south (Cobb & Fix 1987) but this need not trace any dynamical structure. In fact, Figure 7 suggests that sources A and B do not correspond to a bipolar wind encountering a spherical distribution of slowly-moving ejecta. Consequently, one might have to invoke either a fast wind capable of breaking out of the OH toroid in any region of locally reduced density, or a non-spherical distribution of the original PN ejecta, or both. However, Table 2 shows that both sources appear projected in the sky at the same radial distance from the central star. This is consistent with a spherical ejection for the slow wind. The natural direction for any asymmetry of the fast wind or of the original debris would be in the direction roughly

from northwest to southeast of the star, based on the morphology of the H α nebular brightness and the line bisecting sources A and B through the possible weak bridge of emission observed at 13 cm (Fig. 3). There is also evidence for a preferred axis in the same p.a. in the OH velocity slices between -5 and -8 km s $^{-1}$ published by Welty et al. (1987: their Fig. 15). At more negative velocities the OH brightness indicates weaker OH emission along a north-south axis. None of these directions appears to be associated with the nonthermal shock zones.

Strong nonthermal radio continuum emission has also been observed from the OH/IR star OH 326.53-00.419 (also known as D046), with a spectral index of -0.8 . The OH maser emission from D046 occurs over an unusually broad range of 80 km s $^{-1}$ (Sevenster & Chapman 1999; Sevenster & Chapman 2005). D046 appears to represent a post-AGB object, in transition between the AGB and PN phases. These nonthermal emitters may all arise because of the impact of fast winds on circumstellar debris near the end of AGB life. OH 354.88-0.54's intermediate mass progenitor may confer its uniqueness, in that it is still a pulsating long-period variable after it has already created a visible PN, simply because the time scale for stellar evolution is much shorter for a $4 M_{\odot}$ star than for a solar-mass object.

6 CONCLUSIONS

The ionization of the PN associated with OH 354.88-0.54 appears to arise through shock interactions between the AGB star's fast wind and previously ejected cold nebular material. Our discovery of patches of nonthermal radio emission in this PN suggests a kinship with colliding-wind WR binaries but, in OH 354.88-0.54, the two winds were produced by a single central star. The locations of the shocked, nonthermally emitting, regions do not suggest a spherical interaction zone between the winds, nor do they align with any geometrically meaningful direction in the PN itself. However, the nonthermal regions each show the same projected distance from the central star in the plane of the sky, and there is the possibility that faint radio emission links the two regions. These characteristics suggest that the anisotropic fast wind collides with the continuous inner spherical surface of the slow wind. Therefore, this PN offers

a rare opportunity to recognize the nonspherical geometry of the fast wind, close to the time of its onset.

7 ACKNOWLEDGMENTS

The Australia Telescope is funded by the commonwealth of Australia for operation as a National Facility managed by the CSIRO. The MOST is owned and operated by the University of Sydney, with support from the Australian Research Council and Science Foundation within the School of Physics. MC thanks NASA for supporting this work under its Long Term Space Astrophysics and Astrophysics Data Analysis programmes, through grants NAG5-7936 and NNG04GD43G with UC Berkeley. The AAO has undertaken the SHS on behalf of the astronomical community. We thank Jim Caswell, David Frew and Lister Staveley-Smith for valuable discussions.

REFERENCES

- Abbott, D. C., Bieging, J. H., Churchwell, E. 1984, ApJ, 280, 671
 Abbott, D. C., Bieging, J. H., Churchwell, E., Torres, A. V. 1986, ApJ, 303, 239
 Bieging, J. H., Abbott, D. C., Churchwell, E. B. 1989, ApJ, 340, 518
 Becker, R.H., White, R.L., Helfand, D.J., Zoonematkermani, S. 1994, ApJS, 91, 347
 Blöcker, T. & Schönberner, D. 1997, A&A, 324, 991
 Bond, I. A. et al. 2002, MNRAS, 331, L19
 Bridle, A. H. in "Synthesis Imaging in Radio Astronomy", ASP Conf. Ser., 6, 1989, p471. (Eds. R. A. Perley, F. R. Schwab & A. H. Bridle).
 Chapman, J.M., Leitherer, C., Koribalski, B., Bouter, R., Storey, M. 1999, ApJ, 518, 890
 Cobb, M.L., Fix, J.D. 1987, ApJ, 315, 325
 Cohen, M., Parker, Q.A., Chapman, J. 2005, MNRAS, 357, 1189
 Condon, J.J. 1992, ARA&A, 30, 575
 Fitzgerald, M.P. 1968, AJ, 73, 983
 Gaustad, J.E., McCullough, P.R., Rosing, W., Van Buren, D. 2001, PASP, 113, 1326
 Ginzburg, V.L., Syrovatskii, S.I. 1965, Ann.Rev.Astr.Ap., 3, 297
 Green, A. J., Cram, L. E., Large, M. I. and Ye, T., 1999, ApJS, 122, 207
 Iben, I. 1984, ApJ, 277, 333

- Kwok, S., Purton, C.R., Fitzgerald, P.M. 1978, ApJ, 219, L125
- Lang, K.R. 1999, *Astrophysical formulae* (New York: Springer)
- Ledden, J. E., Broderick, J. J., Condon, J. J., Brown, R. L., 1980, AJ, 85, 780
- Leitherer, C., Chapman, J.M., Koribalski, B. 1995, ApJ, 450, 289
- Lucke, P.B. 1978, A&A, 64, 367
- Mezger, P.G., Henderson, A.P. 1967, ApJ, 147, 471
- Neckel, Th., Klare, G., Sarcander, M. 1980, A&AS, 42, 251
- Parker, Q.A. et al. 2005a, MNRAS, 362, 689
- Parker, Q.A., Acker, A., Peyaud, A., Frew, D.J., 2005b, AIP Conf. Proc., 180, 3
- Parker, Q.A. et al. 2006, MNRAS, in press
- Pierce, M.J., 2006, PhD Dissertation, Univ. of Bristol, UK
- Sevenster, M., Chapman, J.M. 1999, ATNF News, Issue 40
- Sevenster, M.N., Chapman, J.M. 2005, in preparation
- Welty, A.D., Fix, J.D., Mutel, R.L. 1987, Ap J, 318, 852
- White, R. L. 1985, ApJ, 289, 698
- White, R.L., Becker, R.H., Helfand, D.J. 2005, AJ, 130, 586
- Zijlstra, A.A., Te Lintel Hekkert, P., Pottasch, S.R., Caswell, J.L., Ratag, M., Habing, H.J. 1989, A&A, 217, 157
- Zoonematkermani, S., Helfand, D.J., Becker, R.H., White, R.L., Perley, R.A. 1990, ApJS, 74, 181